PROCEEDINGS, 50th Workshop on Geothermal Reservoir Engineering
Stanford University, Stanford, California, February 10-12, 2025
SGP-TR-229

Towards Multi-scale Coupled Thermo-Hydro-Mechanical Constitutive Models: Experiments on Thermal Cracking Under Stress with Near-field Acoustic Data

Benjamin HOLTZMAN[1,2,4*], Hoagy O'GHAFFARI[1], Eric BEAUCÉ[2,4], Tushar MITTAL[3], Anna BARTH[4], UIrich MOK[1], Matěj PEČ[1]

1) Earth Resources Lab, MIT; 2) LDEO, Columbia University; 3) Penn State University; 4) Strabo Engineering Inc.

[*]benh@mit.edu

Keywords: Thermal cracking, Thermo-hydro-mechanical coupling, superhot geothermal

ABSTRACT

Thermal cracking may play an important role in fracture network (FN) evolution in geothermal reservoirs. During hydraulic stimulation, boreholes and reservoirs can undergo varying degrees of thermal shock and thermal stress. Thermal cracking, in such situations, may couple strongly with hydraulic and background tectonic stresses to influence seismicity rates and fracture network evolution. In conditions where grain-scale ductility is significant (a.k.a. the brittle-ductile transition), crack tip stresses may be partially relaxed, causing crack interactions to occur at shorter length scales than in the purely brittle field. Thermal stress and cracking may play an important role in creating dense networks of grain-scale fractures. Constitutive models that capture strong coupling among microstructural evolution and thermal, mechanical and hydraulic properties at the grain scale on up are needed to describe high temperature geothermal reservoir processes. We perform tri-axial laboratory experiments at 10 MPa confining pressure, on thermal cracking in Westerly granite. We control stress buildup to varying degrees by ramping up temperature in stages under different mechanical boundary conditions. In some experiments, we lock the piston so that differential stress builds as the sample thermally expands, sometimes to failure levels. In other experiments, we release the stress by retracting the piston between each thermal loading stage. We record continuous near-field acoustic data using novel high-temperature piezoelectric sensors stable up to about 500˚C. Using standard methods of recording acoustic emissions (AEs) by setting triggering levels just above the noise level, we record on the order of several hundred AEs in an experiment. Then, we analyze the continuous data with a signal processing method consisting of short-term/long-term average detections to build a catalog of template waveforms followed by matched filtering. With this approach, we have built a catalog that has about 1000 times more events, mostly below the noise level. We then analyze the temporal clustering statistics of this catalog; we find that the large number of small events are close to random, while small numbers of larger events have strong temporal clustering and cascade-like behavior. Finally, we perform unsupervised feature extraction (using SpecUFEx and hierarchical clustering) to detect/discover temporal patterns in the spectral content of the signals. These show a subtle evolution in the collective sound of fracturing as temperature and stress both increase. While these are initial results, we have found that the combination of near field sensors and high-resolution detection methods show promise for offering new insight and opening new questions into micro-fracturing processes and network evolution.

1. INTRODUCTION

There is a push in the rapidly growing geothermal industry to reach "superhot" conditions (>22 MPa pressure and >375˚C), at which fluids are in a supercritical state. For extracting thermal energy, there are two options: (1) tapping into existing deep hydrothermal convection systems (e.g. Iceland, Japan, New Zealand) and (2) creating new fracture networks in relatively dry regions to make new reservoirs. One of the fundamental challenges with the latter is how to create fracture networks in the deep crust. Mining heat by fluid flow through fracture networks at supercritical conditions has the great advantage that the heat capacity is far higher than water or steam. Less well understood are how fracture networks form and evolve at supercritical conditions– high pressures and, for many rock types, in the broad regime at which grain-scale dissipative mechanisms (e.g. dislocation motion, lattice and grain boundary diffusion) can be activated alongside brittle deformation mechanisms, a.k.a the brittle-ductile transition.

Thermal cracking is understood to arise from (1) stresses that arise from local change in temperature, (2) stress gradients that arise from thermal gradients and (3) internal, local stress concentrations at the grain scale due to thermal expansion anisotropy and thermal expansion mismatch in rocks (e.g. Fredrich and Wong, 1986). A broad range of experiments have been performed to understand thermal cracking in rocks and its consequences for mechanical and transport properties. Among the earliest, to our knowledge, are Wong and Brace (1979); Yong and Wang (1980); Johnston and Toksöz (1980); Bauer and Handin (1983); Fredrich and Wong (1986). In experimental studies, acoustic emissions (AE), nano-seismic events recorded in samples, are taken to be a proxy for cracking events. Yong and Wang (1980) identified that the AE rate is dependent on the heating rate. They interpreted this result not as a direct reflection of the rate, but that higher heating rate causes a steeper thermal gradient and thus higher thermal stress gradients, and thus higher AE rates. They also identified an example of a "Kaiser effect": in thermal cycling, after the first cycle, cracking did not begin again until the temperature reached the peak value of the previous cycle. This phenomenon had been previously identified in cyclic mechanical stress loading in rocks (e.g. Kurita and Fujii, 1979). Wang et al. (1989) found related behavior– an episodic pulsing of AE formation during a monotonic temperature rise in granite of 1˚C per minute. They showed that the temperature at the onset of thermal cracking increases with increasing confining pressure, P_c. This critical temperature can be understood as the existence of a critical stress for thermal cracking, σ^*_{th}, (e.g. Meredith et al., 2001), such that $\sigma^*_{th}(P_c)$, a reduction of elastic modulus, M, with increasing crack density, d_c, i.e. $\partial M/\partial d_c < 0$ (e.g. Schubnel et al., 2006; Nasseri et al., 2009). These two factors can cause non-linearity in the relationship between thermal stress and AE rate through the governing equation for thermal stress $\sigma = \Lambda_{th}\Delta T$, where Λ_{th} is the thermal expansion coefficient, and ΔT is the temperature difference. When that

stress is reached, thermal-elastic strain energy drives cracking until the stress drops below the threshold σ^*_{th}; as the temperature keeps rising, that critical stress will be reached again at a higher temperature. In other words, during the first cracking episode, the critical stress for the undamaged rock is reached at a critical temperature; with a lower elastic modulus, the damaged rock must reach a higher temperature to attain that critical stress. Daoud et al. (2020) also observed a Kaiser effect in coarse grained granitic rocks with complex, interlocking grain boundaries. However, they also showed that fine grained (basaltic) rocks do not crack while temperature is rising, but only on the descending side of a cycle (as grain boundaries fail readily in tension), indicating that grain boundaries and their morphology play an important role in accommodation of thermally-driven local grain-scale stresses.

As thermal cracking occurs, the crack density will affect most of the mechanical properties (e.g. Johnston and Toksöz, 1980; Fredrich and Wong, 1986; Faoro et al., 2013; Nasseri et al., 2007, 2009), heat transport properties (e.g. Wong and Brace, 1979), and fluid transport properties (e.g. Siddiqi and Evans, 2015; Liu et al., 2018; Jones et al., 1997), many of which are coupled, and will also vary significantly if the newly created crack porosity is filled with gas, vapor or fluid. These nonlinear effects will become significantly more complex in the presence of fluids. Hydraulic cracking produces a very different morphology and mechanical behavior than thermal cracking, as illustrated schematically in Fig. 1b. The cracks tend to be larger scale, and have larger spacing (because fluid flow can be much faster than heat diffusion in solids). However, if there is thermal disequilibrium between the fluid and the rock, the two processes will be closely coupled (e.g. Zimmerman, 2000; McTigue, 1986; Ghassemi et al., 2008), as illustrated schematically in Fig. 1b. As they equilibrate, fluid and rock are both changing volume in opposite senses (depending on the sign of $\Delta T_{s-f} = T_s - T_f$).

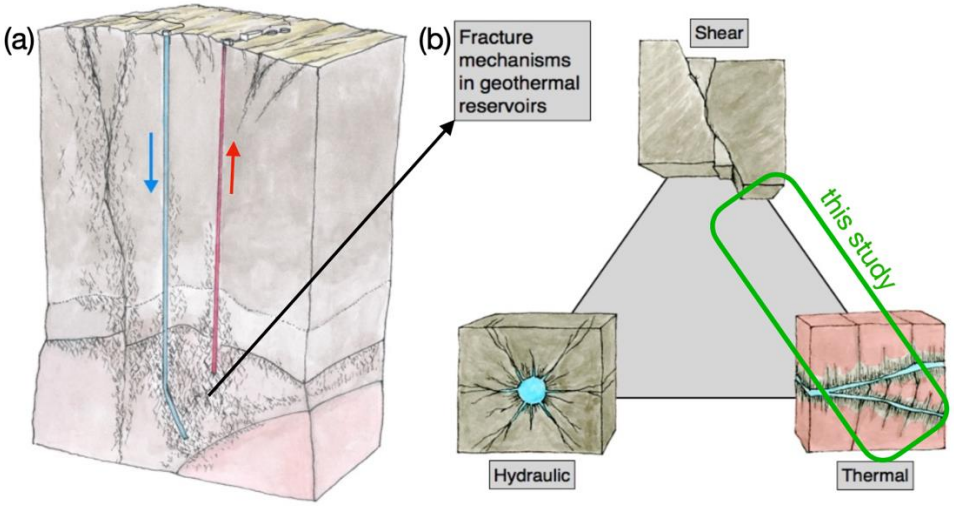

Figure 1(A) geothermal heat mining by tapping an existing hydrothermal system. (B) Fracture forcing map, "shear" refers to far-field stresses such as tectonic and gravitational. Hydraulic and thermal are both local sources. All three forcings can interact at a wide range of scales. The green region shows the subject of this study; fluid-free interactions between thermal and far-field stresses.

As thermal cracking occurs, permeability increases, new surface area becomes available for heat exchange, and the effective elastic modulus and thermal expansion coefficient of the solid decrease. Effective heat transfer coefficients (at a range of length and time scales) may be changing locally in such situations, such that strong coupling and feedbacks may occur. In the conditions of "superhot" geothermal reservoirs that are the target of this work, crustal rocks may be approaching or within the brittle-ductile transition, depending on their bulk composition, microstructure, permeability structure, fluid composition and many other factors (Watanabe et al., 2019; Beeler et al., 2016). Thermal cracking in hot rock experiencing cold thermal shock may be particularly effective at creating permeability (e.g. Watanabe et al., 2019), but there are many open questions on roles of various thermally activated processes, such as viscous relaxation of crack tips, and even the solid framework, that may work to both close and open porosity, locally. Furthermore, in recent experiments by Meyer et al, (2024), they measured permeability while slowly deforming granite samples at a broad range of temperatures. They showed that the fracture networks at high temperature were pervasive and dominated by grain-scale cracks, in contrast to large fractures in the low temperature samples; the higher temperature samples had higher overall permeabilities, with positive implications for deep heat mining. Effective constitutive models are needed that are sufficiently complex to account for these couplings among the mechanical and transport properties during microscopic and mesoscopic fracture network evolution, and their sensitivity to thermodynamic conditions.

In this paper, we present initial results of a new study on the interactions of thermal and applied stresses on the cracking process. We have developed a novel system for (1) high-temperature, near-field "needle" sensors that sit directly upon the sample, in the hot zone of the furnace, enabling unprecedented proximity to the deformation processes at high temperature conditions, and (2) a new signal processing workflow for high resolution detection of acoustic emissions (AEs) from the continuous data recorded by the near-field sensors. Initial results from this combination are presented here. We then apply statistical analyses of temporal clustering and unsupervised pattern discovery methods to the high-resolution AE catalogs. For this study, even though the ultimate aim is to understand fluid flow and heat extraction, we start with fluid-absent conditions, to try to better understand the fracture behavior as interactions of thermal (local) and mechanical boundary conditions, as an analogue for far-field stresses.

2. EXPERIMENTAL METHODS AND DESIGN

2.1 Experimental Design

The thermal cracking experiments are performed in a Paterson Instruments Gas-medium Deformation Apparatus at MIT ("PI-5") (#5 of 13 in the world), illustrated in Fig. 2a. We deform Westerly Granite (among the most extensively studied reference materials for the continental crust, e.g. Tullis and Yund, 1977). Experiments are performed at 10 MPa confining pressure (Pc), applied by argon gas in the pressure vessel chamber around the sample assembly (Fig. 2b). The samples are small, 10 mm diameter by 20 mm long, but the mean grain size in our samples is about 0.5 mm, so individual grains will not dominate the sample behavior.

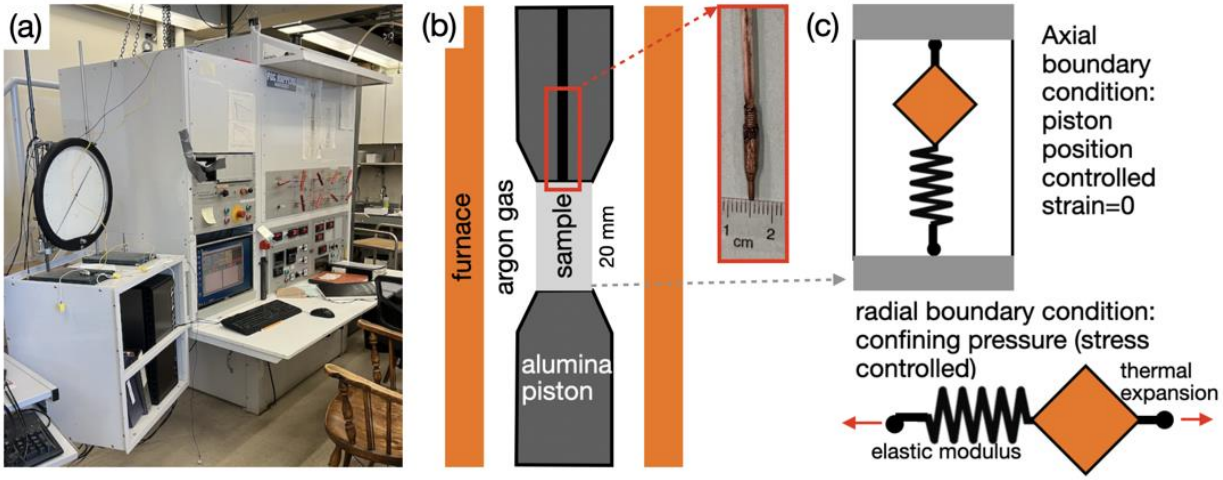

Figure 2(a) Paterson Instruments Gas Medium Deformation Apparatus, PI-5 at MIT. (b) Sample assembly in the furnace hot zone. The piezoelectric transducer (PZT, inset) is sitting in what is usually the thermocouple hole in the piston. (c) The thermoelastic phenomenological model can be conceptually viewed as strain controlled in the axial direction and stress (or pressure)-controlled in the radial direction. P_c=10 MPa in these experiments.

2.2 High Temperature, Near-field Acoustic Sensors

The Paterson machine was not designed for piezoelectric transducers (PZTs), i.e. acoustic sensors, so we have modified the sample assembly to incorporate PZTs in the hot zone, as shown in Fig. 2b,c. Other Paterson instruments have been outfitted with PZTs, in the far field (e.g. Burlini et al., 2007), outside the hot zone of the furnace. Such piezoelectric sensors are not stable above about 200 ºC, made of piezo-ceramics PZT-5A. Our high-temperature near-field "needle" sensors are unique, made of Bismuth Titanate (HG-IT-2023: Ferroperm Pz46 Bismuth Titanate) crystals, and patented (O'Ghaffari and Peč, 2023), illustrated in Fig. 2c. These sensors have a frequency band of about 70kHz to 18 MHz, with a resonance frequency of 2.25 MHz.

We performed six experiments, mainly testing different sensors and experimental boundary conditions. There were extensive electromagnetic noise problems from multiple sources, but they have been solved. We were able to record triggered and continuous data with two data acquisition de- vices and to de-noise acoustic data from experiments e1 and e6 (Fig. 3), with clear detections in a triggered catalog. Our attempts to include a thermocouple in addition to the PZT crystal were plagued by probably unrelated noise sources.

(a)

experiment #	boundary cond.	AE detections
1 (#056)	heat->release	triggered + continuous data
6 (#063)	heat->hold	triggered only

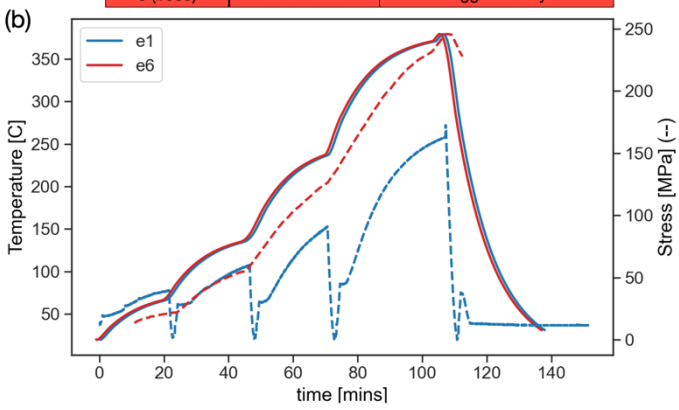

Figure 3 Experimental conditions and thermal-mechanical paths. (a) Table of experiments, with color key. (b) Temperature paths (solid) and resulting stress paths (dashed).

2.3 Thermo-mechanical Boundary Conditions

The samples were heated along different paths by increasing the furnace power input in increments of 10% quickly (<30 s) and holding that power level for about 20-30 minutes, leading to sequential rapid rises of temperature increase rates that taper off, as shown in Fig. 3b. We used the temperature data from experiments with a thermocouple **(e2-e5**) to constrain a model of the furnace behavior, for experiments without a thermocouple (**e1** and **e6**). We integrate an ODE of the form $\dot{\theta} = \frac{P_f(t)}{C_{eff}(P_f)} - \frac{\theta}{\tau_{th}}$, where θ is temperature above the initial temperature (25 ºC), and $\dot{\theta}$ is the rate of temperature change [ºC/s]. The furnace power time series $P_f(t)$ is the control function, $C_{eff}(P_f)$ is a constant that is fit independently for each power step, and the thermal relaxation time τ_{th} is extracted from the cooling path. The results are shown in Fig. 3b.

The stress accumulation caused by thermal expansion of the sample was strongly influenced by the boundary conditions, shown in Fig. 2c. The piston position was controlled and fixed in place, amounting to "strain-control" in the axial direction, and "stress-control" by the fixed confining pressure in the radial direction. For some experiments, the piston was locked during the entire experiment ("heat→hold" in the table in Fig. 3a); in others, the piston position was fixed during heating steps, but the stress was relaxed between heating steps by moving the piston away and then re-touching the sample before starting the next heating step ("heat→release"), which cause different stress paths for the same heating path.

3. RESULTS

Here, we describe the results from the mechanical data and microstructures, followed by the acoustic data analysis methods and results. These are initial results, from experimental and data-analytical methods that are still in development, but there are already interesting patterns and questions that have emerged.

3.1 Mechanical Data

Two example temperature-stress paths are shown in Fig. 3. The 10% increases in furnace power produce rapid increases in temperature with decreasing rate. As shown in Fig. 3b), the stress paths for the heat->hold experiment (**e6**) track the temperature paths closely, while the heat->release experiment (**e1**) reaches a much lower total stress, by relaxing between each heating step. This approach lets us compare very different thermodynamic paths with a simple change in the boundary conditions. The heat→hold experiments reach a yield stress followed by clear weakening, i.e. the sample failed.

3.2 Microstructures

Fig. 4a,b,c show scanning electron microscope (SEM) images of the full samples for the starting material, **e1** and **e3** (**e3** experienced a very similar path to **e6**, and both **e3** and **e6** reached failure). Initial measurements of fracture density show that the starting material has very low fracture density (~1.3 mm^2/mm^3), the sample **e1** that did not fail has clear grain scale fractures, many of which do not appear to be connected, in the inset of Fig 4b shown in Fig 4d. In contrast, the sample **e3** developed a clear cross-cutting fault associated with the failure, and has a much higher fracture density in the vicinity of the fault, shown in Fig. 4e. This through-going fault developed presumably late in the experiment, most likely associated with the drop in stress seen in Fig. 3b. The fracture density appears to be higher above the fault than below, at least in the near-fault region. Fractures are both intra-granular and running along grain- and phase-boundaries. The relative connectivity of these fracture networks at this scale remains to be determined. Note that there is minimal *macroscopic* axial strain associated with this rupture (other than the elastic deformation of the entire sample assembly), but significant radial strain, as the piston positions are fixed.

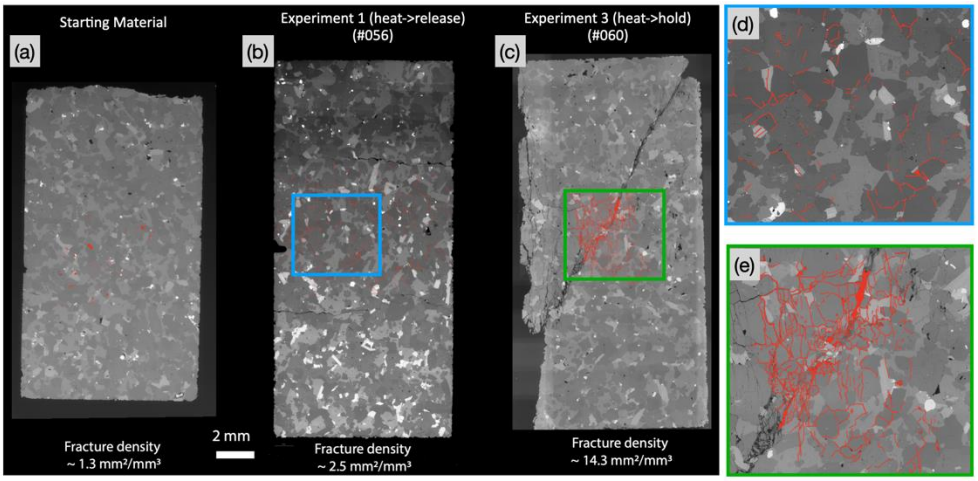

Figure 4 Scanning electron microscope (SEM) images of microstructures using back-scattered electrons (BSE) from (a) the starting material (b) expt. 1 (056) that did not fail, (c) expt. 3 that did fail, with a large, cross-cutting shear rupture. (d) zoom in on fracture density map from e1, and (e) fracture density map of e3.

3.3 Acoustic data processing and AE catalog production

Here, we describe the triggered detection (TD) method and results from the near-field, high T acoustic sensors, followed by high-resolution detection (HRD) methods and results. We then analyze those data further with temporal clustering statistics and unsupervised feature extraction and pattern discovery.

3.3.1 Triggered Catalogs

The standard method for detecting and recording AEs involves simply recording a waveform when the amplitude is above a manually set trigger level above the noise level (then removing "events" that are single pulses, which here are electromagnetic pulses from the furnace circuitry). This method is implemented during each experiment for which the background noise levels were low enough, namely **e1** and **e6**. These catalogs are shown in Fig. 5a,b, with 126 events for **e1** and 251 for **e6**. The dot sizes are scaled as relative peak amplitudes of the events, but they cannot be compared between experiments.

These triggered events are recorded at 1 GHz sampling rate to see the broad range of frequencies, which is only possible for short signals, not continuous data. An example waveform from **e1** (red circle) and its spectrum are shown in Fig. 5c,d. The power is highest around 1 MHz; the decay at higher frequencies may be a combination of the sensor characteristics, attenuation and the source spectra. Fig. 5e shows a sequence of spectra of events from **e1** increasing in temporal sequence from the bottom up. The red band indicates the time in the experiment after which the spectra begin to show higher frequency content.

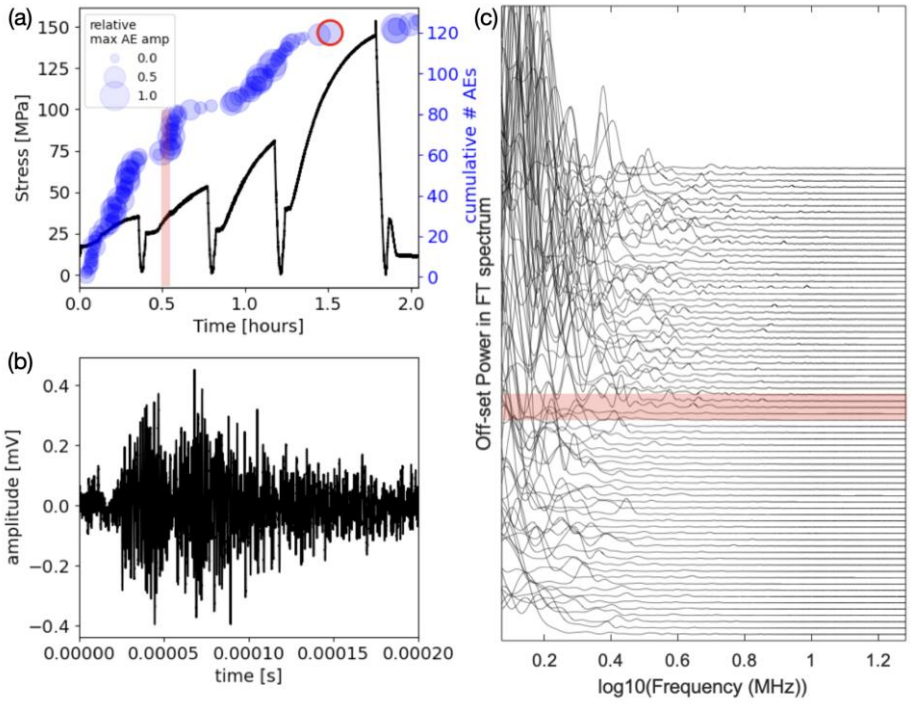

Figure 5 Example triggered AE catalog (a) expt. 1 catalog of 126 events, plotting stress (black) and AE relative amplitude for all events (blue). (b) An example waveform, for the red circle event in (a) (c) amplitude spectra for 75 events in expt. 1 above ~ 1 MHz. Events are ordered in time with earliest event at base, last event at top. Red band indicates an increase in frequency content, likely with increasing damage. This red band corresponds to ~0.5 hours (see red band in (a)).

3.3.2 High Resolution Catalogs

The standard triggered approach, while conveniently dealing with data storage limitations, misses weak AE activity that encodes important information about the physical state and the dynamics of the system. Here, we leverage continuous acoustic recordings and modern detection techniques, developed in the context of earthquake seismology, to produce high resolution AE catalogs. Beaucé et al., (2024) developed methods for high resolution earthquake detection and location, which are adapted here for single-channel recording, in the following steps:

- Initial detection: We use the short-term average/long-term average (STA/LTA) technique to detect events above noise level and build an initial database of AEs (removing electrical noise pulses if necessary).
- High resolution detection: We densify the initial catalog with matched filtering (MF), that is, correlating the waveforms of the initially detected events with the continuous recordings. This correlation-based technique detects new, potentially very weak events that are similar to their template event. MF is a computationally intensive task for which we have developed GPU-accelerated software (Beaucé et al., 2018).

For experiment 1, this method detected about 271,744 events at a MF detection threshold of 5x the RMS of the correlation coefficient (CC) time series (about 1000 times more than triggered catalog). This detection threshold is low but stacking 100 of the strongest (highest CCs) or of the weakest (lowest CCs) detections produces a waveform closely similar to the template (see Figure 6b), thus demonstrating that weak detections are small acoustic emissions. The number of detected events is highly dependent on the detection threshold. For example, raising the threshold to 6.5x the RMS gives a much smaller number of 213 events (Figure 6c). In the following, we present an analysis of our catalog filtered at different detection thresholds.

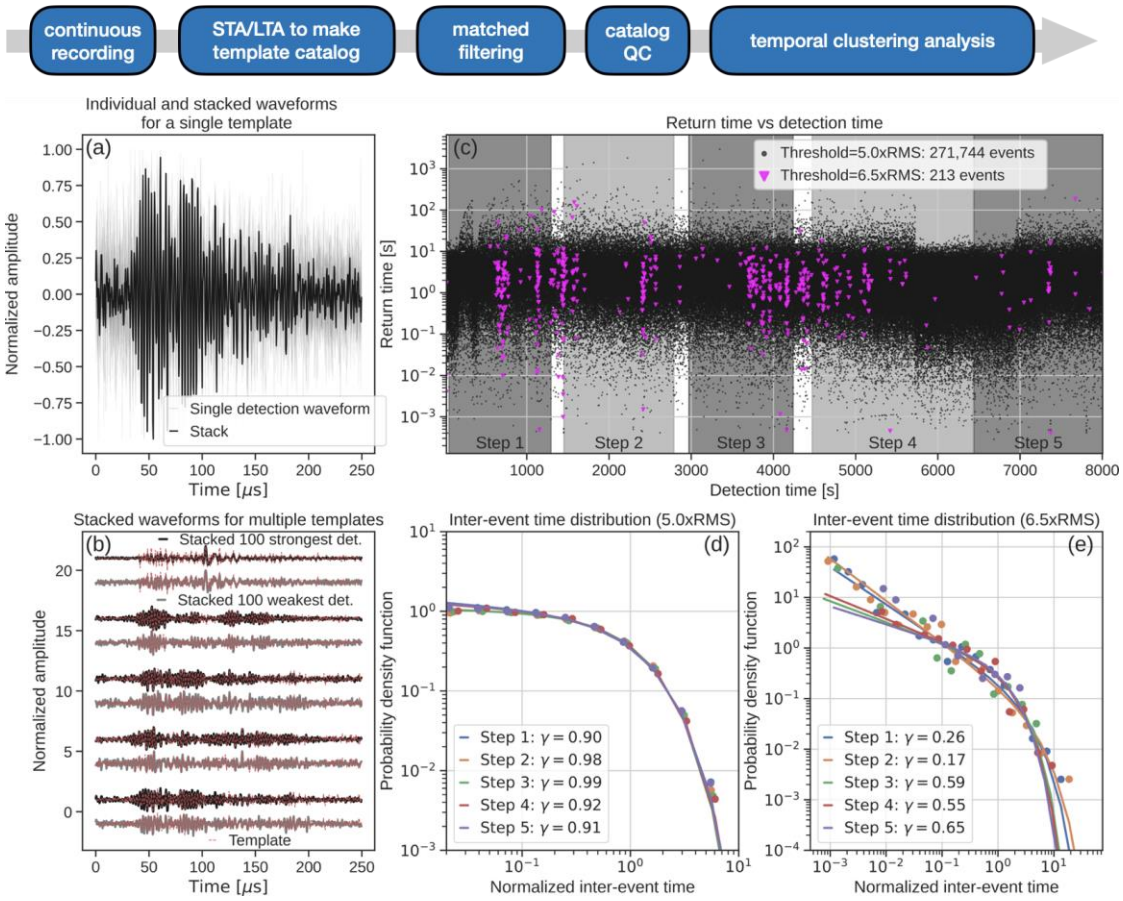

Figure 6 High resolution detections on continuous data from expt. 1. Top: the workflow. (a) a single detected waveform (light grey) and the stack of all waveforms detected from a single template (black). The template waveform itself (not shown) corresponds closely to the stack. (b) The 100 highest and lowest correlated events stacked, overlain by the template in red, for 5 randomly selected templates. Many of these detected events are well below the noise level, and only appear when stacked. (c) High resolution catalogs including events above two thresholds above the RMS of all cross-correlation coefficients, 5.0 and 6.5. The higher threshold catalog, shown with triangles, contains 213 events, similar to the triggered catalog; the 5.0xRMS catalog has 271,744 events. The grey bins correspond to thermal loading (or stress) steps shown in Fig 3. (d) and (e) show the log probability distributions for the log of the interevent times, fitted by the gamma model, for the two catalogs for 5.0 and 6.5xRMS. The very different distributions indicate that the lower detection threshold is very close to Poissonian ($\gamma = 1$), random recurrence times, unclustered in time, while the higher detection threshold catalog is strongly clustered ($\gamma << 1$). Furthermore, while there is noise in these data, there is a general increase in γ, or decrease in clustering, with increasing temperature and stress.

3.3.4 Temporal Clustering Statistics

The temporal statistics of events encode the physics of their interactions: weakly clustered or random (e.g., Poissonian) occurrences indicate that when events nucleate in response to some external forcing, they do not significantly interact with other events, whereas strongly clustered occurrences indicate cascading caused by subsequent perturbations of the stress field due to the events themselves (e.g., Marsan and Lengliné, 2008; Beaucé et al., 2022). Strong clustering may be promoted by the properties of the fracture network or by the stress mediating properties of the rock, that is, its rheology. Here, we systematically characterize the statistics of the AE occurrences by fitting a gamma law to the distribution of inter-event times τ: $p(\tau;\gamma;\beta) = C\tau^{\gamma-1}e^{-\tau/\beta}$ (e.g. Hainzl et al., 2006; Marsan et al., 2013), with results shown in Fig. 6d,e. The model parameter, γ, varies between 1 (Poissonian, unclustered occurrences) and 0 (fully clustered occurrences). Our goal is to discover relationships between the event statistics and the physical state and properties of the sample throughout time. We found that weak detections (mostly small events) tend to behave randomly whereas strong detections (mostly large events) exhibit much more clustering (see Figure 6d,e). This result suggests that small AEs are driven by the pervasive microcracking due to thermal stressing while large AEs are part of cascading brittle failure, and opens many new questions.

3.4 Unsupervised Pattern Discovery

3.4.1 Methodology (SpecUFEx+Hierarchical Clustering)

The aim of our unsupervised learning approach applied here is to extract subtle variations in the frequency content through time of all the signals. The method used here, called SpecUFEx, operates on spectrograms (though other time-frequency representations such as wavelet transform periodograms could be used). The full details of SpecUFEx may be found in Holtzman et al., (2018), applied to microseismicity from The Geysers, and Sawi et al., (2022), applied to icequakes in the Gorner Glacier. Briefly, this method involves a number of dimensionality-reducing pattern-enhancing steps to transform each spectrogram into a fingerprint. First, nonnegative matrix factorization (NMF) is applied to spectrograms of the AE waveforms to split each spectrogram into a dictionary of frequency components (common to all events) and a matrix of activation coefficients (unique for each event). Hidden Markov models (HMMs) are then learned on the NMF activation matrices to further reduce dimensionality and highlight temporal patterns; each NMF matrix is represented as a sequence of hidden states in time, where states are patterns of frequency components. The fingerprints are generated by counting transitions between states in time.

Following the NMF-HMM sequence, we perform hierarchical agglomerative clustering on the fingerprints to identify groups of fingerprints with similar characteristics. We choose a number of clusters (based on criteria discussed below). Once each fingerprint is assigned to a cluster, we can then plot the number of events from each cluster over time (Figure 7c).

The final dimensionality-reduction step is to count the number of transitions between events in each cluster for each temperature step of the experiment (Figure 7d). The result is a matrix for each stress step of the current state versus the previous state, with color indicating the number of times that transition occurred during the stress step. We call these Cluster tRAnsition Matrices, or CRAMs. This figure is thus a graph-representation of the transitions in the frequency content of the acoustic emission catalog. When separated out by time segments, in this case, heating steps, they illustrate subtle changes in the collective sounds of the fracture network evolution.

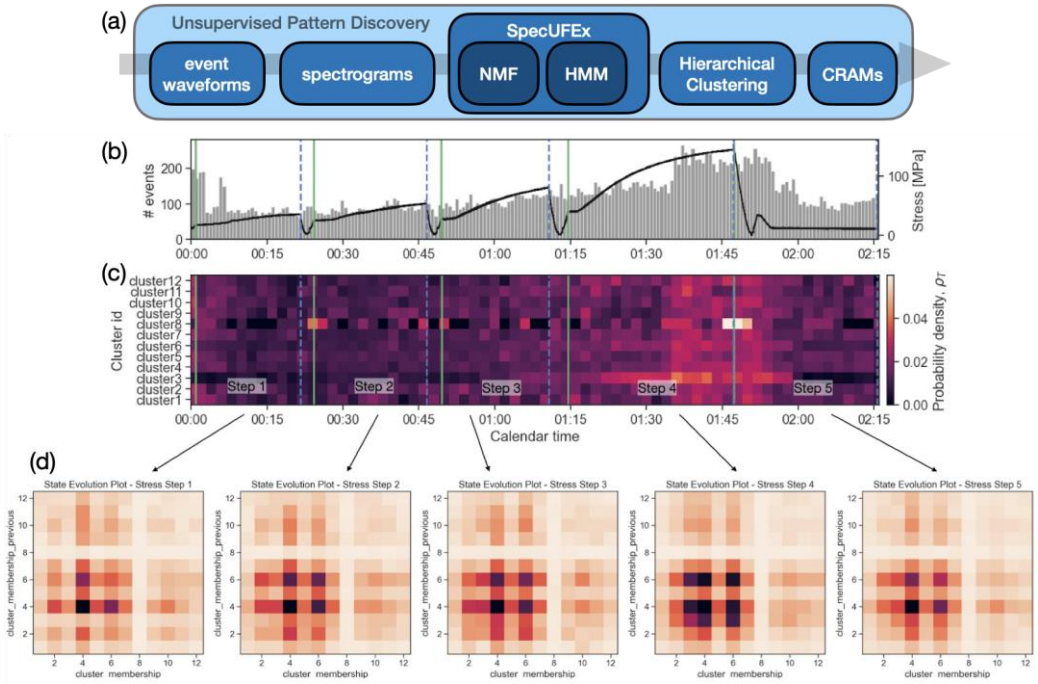

Figure 7 Unsupervised Pattern Discovery using SpecUFEx feature extraction and hierarchical clustering. (a) workflow (b) histogram of the # of events for the 5.5xRMS catalog (~25,000 total events), and the stress, with steps indicated by green (start) and blue dashed (end) lines. (c) Time histograms (normalized by rows) for each of the 12 clusters, and (d) their associated CRAMs for each stress step (note that each CRAM is normalized so absolute colors should not be compared between CRAMS). The CRAMs show subtle but systematic changes with increasing stress and temperature for each step, and the final step is the quench of the sample.

3.4.2 Unsupervised Pattern Discovery Results

While the silhouette score for this dataset from 2 to 25 clusters shows that 6 clusters capture most of the separation, we show results for 12 clusters, to provide more richness in the CRAMs. The temporal patterns shown in Figure 7c are not strong and thus difficult to interpret in this case. However, the reduction into CRAMs reveals subtle pattern. There is a general trend towards more intense concentrations in the lower left over the four stress/temperature steps. Note that more events were detected in between steps 3 and 4 because of a slight shift in the amplifier gain during the experiment, also visible in the interevent times in Fig. 6c, and the more frequent occurrence of each cluster (brighter colors in Fig. 6c). This shift does not affect the CRAMs due to their normalization; it is not what causes the change from segments 4 to 5. That shift is more likely due to increasing thermal stress as the sample is expanding, to a sudden shift to contraction during the quench of the sample: the collective sound of cracking during the quench is different than that of the peak thermal stress.

4. DISCUSSION

We have demonstrated that placing a near-field sensor on a deforming sample and applying high-resolution event detection methods provides a novel view into the processes occurring inside the sample and opens many questions. Unfortunately, due to a variety of noise sources (that we have now isolated), we were only able to build a high-resolution catalog for one experiment (**e1**). Thus, we are limited in how much we can speculate on the meaning of the detected patterns, and their potential for an improved understanding of thermal cracking and its interactions with ambient stress fields. However, interesting questions have arisen from the results of one experiment.

The first order pattern from the temporal clustering analysis is that the very numerous small magnitude events detected below the noise level are close to random (γ approaching 1); these probably reflect local internal stress mismatches (e.g. Fredrich and Wong, 1986) popping off randomly as the sample heats up. In contrast, the larger events (strong detections) are strongly clustered in time, suggesting cascading, interacting events. A general model for large-scale brittle failure predicts the progressive coalescence of brittle deformation onto a highly localized 2D structure (Girard et al., 2010; Renard et al., 2017), leading us to think that the AE temporal clustering informs on the likelihood of large-scale brittle failure. In experiment 1, thermal stresses did not build enough to lead to the macroscopic failure of the sample, because we deliberately relaxed the stress between each heating step. In experiments 3 and 6, we locked the piston and they failed. Therefore, we would expect temporal clustering to increase over time in the latter two. Further experiments in which the samples are stressed to failure will help to test this conjecture.

The second order pattern in the strong detections (>6.5xRMS in Fig. 6e) is that as temperature increases, temporal clustering in the strong detections is less and less prominent; that is, γ generally increases with each stress step. In this sequence, those steps are increasing both in temperature and stress (but lower stress than if we had locked the piston). We therefore hypothesize that the decrease in clustering is due to the effects of increasing temperature, for example, by causing a decrease in the ability of cracks to interact because of local relaxation of their stress concentrations, or, a tendency for cracks to remain corralled along grain boundaries and thus not form larger, throughgoing cracks. If the stress were higher, the potential for cracks to overcome these local relaxations would be greater. We can cast these different paths as a competition between temperature (or entropy) and stress in the patterns of dissipation of free energy, as the samples enter the brittle-ductile transition.

This result is reminiscent of the behavior of synthetic earthquakes in a damage rheology model (Ben-Zion and Lyakhovsky, 2006): at low temperatures, the system dissipates energy through brittle failure cascading (i.e., AE clustering) whereas at higher temperatures ductile processes take over. Temperature is, however, not the only factor controlling rheology. The dominant dissipation process is a function of both temperature and a number of other state variables, including the full stress- and damage state. Monitoring AE clustering throughout time gives us insights into the propensity of a system for brittle failure cascading along a certain temperature/stress path. How do these patterns depend on heating rate, on present damage state, on grain size and the nature of a rock's grain boundaries and other aspects of its internal complexity? These questions have important implications for the understanding of the development of crack networks in geothermal reservoirs, as well as for seismic safety monitoring protocols.

Rich information about the mechanical behavior of a system is encoded in the acoustic/seismic wavefield (Campillo and Paul, 2003; Brenguier et al., 2008; Beaucé et al., 2023; O'Ghaffari et al. 2023b) and our capacity to decipher this wavefield remains limited. Machine learning has been offering new tools to tap into this encoded information to characterize and understand geosystems (e.g., Rouet-Leduc et al., 2017; Holtzman et al., 2018). Our unsupervised machine learning methodology aims to find patterns in complex signals that we can relate to the mechanical behavior of the system at given temperature and stress conditions. While the CRAM patterns in experiment 1 are fairly subtle, we expect that they will be quite different from those in an experiment that approached and reached failure, just as the fracture networks shown in Fig. 4 are very different between the sample that failed and the one that did not. One of our broader aims is to move from unsupervised pattern discovery to the determination of labels that are characteristic of the state of a system and its near-future evolution, building on the pioneering work of Rouet-Leduc et al., 2017. Further work will reveal the potential for these approaches.

5. CONCLUSIONS

We have shown first results of high-resolution acoustic emission catalogs built from continuous recordings from near-field, high temperature sensors. Interesting questions have arisen on the interactions of numerous microfractures that are randomly occurring, and the fewer, larger events with strong temporal clustering. With further experiments, we believe these methods will constitute a step towards a better understanding of evolving microfracture networks in the deep crust, and eventually how to control them for deep heat mining.

ACKNOWLEDGEMENTS

This work was funded by DOE Basic Energy Sciences seed grant DE-SC0024678 entitled "Towards machine-learning a fully-coupled constitutive model for thermal-hydraulic fracture in geothermal systems: phase I" to B. Holtzman. We also acknowledge support from the "Science Foundations for the Energy Earthshots" grant DE-SC0024937 to the MARBLE-C project, PI S. Saltiel (Cornell Univ., sub-award to A. Barth, Strabo Engineering). "CORD" Laboratory technician support by NSF-2054414 to M.P. is gratefully acknowledged. BH, EB and AB have financial interest in Strabo Engineering Inc.

REFERENCES

Bauer, S. J. and Handin, J. (1983). Thermal expansion and cracking of three confined water-saturated igneous rocks to 800 C. *Rock Mechanics and Rock Engineering, 16*(3):181–198.

Beaucé, E., Frank, W. B., & Romanenko, A. (2018). Fast matched filter (FMF): An efficient seismic matched-filter search for both CPU and GPU architectures. *Seismological Research Letters, 89*(1), 165-172.

Beaucé, E., van der Hilst, R. D., & Campillo, M. (2022). Microseismic constraints on the mechanical state of the North Anatolian fault zone 13 years after the 1999 M7.4 Izmit earthquake. *Journal of Geophysical Research: Solid Earth*, *127*(9), e2022JB024416.

Beaucé, E., Poli, P., Waldhauser, F., Holtzman, B., & Scholz, C. (2023). Enhanced tidal sensitivity of seismicity before the 2019 magnitude 7.1 Ridgecrest, California earthquake. *Geophysical Research Letters*, *50*(14), e2023GL104375.

Beaucé, E., Frank, W. B., Seydoux, L., Poli, P., Groebner, N., van der Hilst, R. D., & Campillo, M. (2024). BPMF: A Backprojection and Matched-Filtering Workflow for Automated Earthquake Detection and Location. *Seismological Research Letters*, *95*(2A), 1030-1042.

Beeler, N., Hirth, G., Thomas, A., and B¨urgmann, R. (2016). Effective stress, friction, and deep crustal faulting. *Journal of Geophysical Research: Solid Earth, 121*(2):1040–1059.

Ben-Zion, Y., & Lyakhovsky, V. (2006). Analysis of aftershocks in a lithospheric model with seismogenic zone governed by damage rheology. *Geophysical Journal International*, *165*(1), 197-210.

Brenguier, F., Shapiro, N. M., Campillo, M., Ferrazzini, V., Duputel, Z., Coutant, O., & Nercessian, A. (2008). Towards forecasting volcanic eruptions using seismic noise. *Nature Geoscience*, *1*(2), 126-130.

Burlini, L., Vinciguerra, S., Di Toro, G., De Natale, G., Meredith, P., & Burg, J. P. (2007). Seismicity preceding volcanic eruptions: New experimental insights. *Geology*, *35*(2), 183-186.

Campillo, M., & Paul, A. (2003). Long-Range Correlations in the Diffuse Seismic Coda. *Science*, 299, 547-549.

Daoud, A., Browning, J., Meredith, P. G., and Mitchell, T. M. (2020). Microstructural controls on thermal crack damage and the presence of a temperature-memory effect during cyclic thermal stressing of rocks. *Geophysical Research Letters, 47*(19):e2020GL088693.

Faoro, I., Vinciguerra, S., Marone, C., Elsworth, D., and Schubnel, A. (2013). Linking permeability to crack density evolution in thermally stressed rocks under cyclic loading. *Geophysical Research Letters, 40*(11):2590–2595.

Fredrich, J. T. and Wong, T.-f. (1986). Micromechanics of thermally induced cracking in three crustal rocks. *Journal of Geophysical Research: Solid Earth, 91*(B12):12743–12764.

Ghassemi, A., Nygren, A., and Cheng, A. (2008). Effects of heat extraction on fracture aperture: A porothermoelastic analysis. *Geothermics, 37*(5):525–539.

Girard, L., Amitrano, D., & Weiss, J. (2010). Failure as a critical phenomenon in a progressive damage model. *Journal of Statistical Mechanics: Theory and Experiment*, *2010*(01), P01013.

Hainzl, S., Scherbaum, F., & Beauval, C. (2006). Estimating background activity based on interevent-time distribution. *Bulletin of the Seismological Society of America*, *96*(1), 313-320.

Holtzman, B. K., Paté, A., Paisley, J., Waldhauser, F., and Repetto, D. (2018). Machine learning reveals cyclic changes in seismic source spectra in geysers geothermal field. *Science Advances, 4(5)*:eaao2929.

Johnston, D. H. and Toks¨oz, M. N. (1980). Thermal cracking and amplitude dependent attenuation. *Journal of Geophysical Research: Solid Earth, 85*(B2):937–942.

Jones, C., Keaney, G., Meredith, P., and Murrell, S. (1997). Acoustic emission and fluid permeability measurements on thermally cracked rocks. *Physics and Chemistry of the Earth, 22*(1-2):13–17.

Kurita, K. and Fujii, N. (1979). Stress memory of crystalline rocks in acoustic emission. *Geophysical Research Letters, 6*(1):9–12.

Liu, J., Li, B., Tian, W., and Wu, X. (2018). Investigating and predicting permeability variation in thermally cracked dry rocks. *International Journal of Rock Mechanics and Mining Sciences, 103*:77–88.

Marsan, D., & Lengline, O. (2008). Extending earthquakes' reach through cascading. *Science*, *319*(5866), 1076-1079.

Marsan, D., Prono, E., & Helmstetter, A. (2013). Monitoring aseismic forcing in fault zones using earthquake time series. *Bulletin of the Seismological Society of America*, *103*(1), 169-179.

McTigue, D. (1986). Thermoelastic response of fluid-saturated porous rock. *Journal of Geophysical Research: Solid Earth, 91*(B9):9533–9542.

Meredith, P. G., Knight, K. S., Boon, S. A., and Wood, I. G. (2001). The microscopic origin of thermal cracking in rocks: An investigation by simultaneous time-of-flight neutron diffraction and acoustic emission monitoring. *Geophysical research letters, 28*(10):2105–2108.

Meyer, G. G., Shahin, G., Cordonnier, B., & Violay, M. (2024). Permeability partitioning through the brittle-to-ductile transition and its implications for supercritical geothermal reservoirs. *Nature Communications*, *15*(1), 7753.

Nasseri, M., Schubnel, A., Benson, P., and Young, R. (2009). Common evolution of mechanical and transport properties in thermally cracked westerly granite at elevated hydrostatic pressure. *Pure and applied geophysics, 166*(5-7):927–948.

Nasseri, M., Schubnel, A., and Young, R. (2007). Coupled evolutions of fracture toughness and elastic wave velocities at high crack density in thermally treated westerly granite. *International Journal of Rock Mechanics and Mining Sciences, 44*(4):601–616.

O'Ghaffari, H. and M. Peč (2023). "High-temperature miniature ultrasonic probes" US Patent WO2024097017A1.

O'Ghaffari, H., Peč, M., Mittal, T., Mok, U., Chang, H., & Evans, B. (2023b). Microscopic defect dynamics during a brittle-to-ductile transition. Proceedings of the National Academy of Sciences, 120(42), e2305667120.

Renard, F., Cordonnier, B., Kobchenko, M., Kandula, N., Weiss, J., & Zhu, W. (2017). Microscale characterization of rupture nucleation unravels precursors to faulting in rocks. *Earth and Planetary Science Letters*, *476*, 69-78.

Rouet-Leduc, B., Hulbert, C., Lubbers, N., Barros, K., Humphreys, C. J., & Johnson, P. A. (2017). Machine learning predicts laboratory earthquakes. *Geophysical Research Letters*, *44*(18), 9276-9282.

Sawi, T., Holtzman, B., Walter, F., & Paisley, J. (2022). An Unsupervised Machine-Learning Approach to Understanding Seismicity at an Alpine Glacier. *Journal of Geophysical Research: Earth Surface*, *127*(12), e2022JF006909.

Schubnel, A., Benson, P. M., Thompson, B. D., Hazzard, J. F., and Young, R. P. (2006). Quantifying damage, saturation and anisotropy in cracked rocks by inverting elastic wave velocities. In *Rock damage and fluid transport, part I, Pageoph Special Issue*, pages 947–973. Springer.

Siddiqi, G. and Evans, B. (2015). Permeability and thermal cracking at pressure in sioux quartzite. *Geological Society, London, Special Publications*, *409*(1):49–66.

Tullis, J., & Yund, R. A. (1977). Experimental deformation of dry Westerly granite. *Journal of geophysical research*, *82*(36), 5705-5718.

Wang, H. F., Bonner, B. P., Carlson, S. R., Kowallis, B. J., and Heard, H. C. (1989). Thermal stress cracking in granite. *Journal of Geophysical Research: Solid Earth*, *94*(B2):1745–1758.

Watanabe, N., Sakaguchi, K., Goto, R., Miura, T., Yamane, K., Ishibashi, T., Chen, Y., Komai, T., and Tsuchiya, N. (2019). Cloud-fracture networks as a means of accessing superhot geothermal energy. *Scientific reports*, *9*(1):1–11.

Wong, T.-f. and Brace, W. (1979). Thermal expansion of rocks: some measurements at high pressure. *Tectonophysics*, *57*(2-4):95–117.

Yong, C. and Wang, C.-y. (1980). Thermally induced acoustic emission in westerly granite. *Geophysical research letters*, *7*(12):1089–1092.

Zimmerman, R. (2000). Coupling in poroelasticity and thermoelasticity. *International Journal of Rock Mechanics and Mining Sciences*, *37*(1-2):79–87.